Mapping the Exit Route of Hydrogen Peroxide From the Manganese Superoxide Dismutase (MnSOD) Active Site.

Medhanjali Dasgupta[a], Katelyn Slobodnik[a], Erika A. Cone[a], Jahaun Azadmanesh[a], Thomas Kroll[b], Gloria E. O. Borgstahl[a]*

[a] Eppley Institute for Research in Cancer and Allied Diseases, 986805 Nebraska Medical Center, Omaha, NE, 68198-6805, USA.

[b] Stanford Synchrotron Radiation Lightsource, SLAC National Accelerator Laboratory, Menlo Park, CA, 94025, USA.

*Corresponding author at: Eppley Institute for Research in Cancer and Allied Diseases, 986805 Nebraska Medical Center, Omaha, NE 68198-6805, USA.

Email address: gborgstahl@unmc.edu (Gloria E. O. Borgstahl)

Abstract

Mitochondrial manganese superoxide dismutase (MnSOD) converts superoxide ($O_2^{\bullet-}$) into hydrogen peroxide (H_2O_2) and molecular oxygen (O_2), serving as a key defense against oxidative damage. Despite decades of research, the product exit pathway in MnSOD remains understudied, due to the enzyme's rapid, diffusion-limited catalysis. Here, we structurally characterize the H_2O_2 exit route in MnSOD, using a kinetically impaired Gln143Asn variant. In the wild-type enzyme, Gln143 participates in proton transfer reactions with the Mn^{3+}-bound solvent (WAT1) to drive redox cycling of the metal for effective $O_2^{\bullet-}$ dismutation. Substitution with Asn disrupts the proton transfer, as Asn is too far away from WAT1, and stalls redox transitions in the Gln143Asn variant. This generates a "slow-motion" version of catalysis that maximizes the likelihood of trapping and visualizing the H_2O_2 exit process with improved experimental control. Results reveal that the Gln143Asn substitution introduces a cavity, which permits conformational flexibility of Tyr34, that would be sterically disallowed in the wild-type. This flexibility of Tyr34 narrows the gateway between the second-shell residues Tyr34 and His30 and restricts diffusion of the Mn^{2+}-bound peroxide out of the metal's primary coordination sphere. Also, peroxide occupies a secondary binding site between Tyr34 and His30. The combination of Tyr34 flexibility and the enzyme's inability to redox cycle causes a "traffic jam" of peroxide at the mouth of the blocked gateway. Overall, our findings provide novel structural insight into the mechanism of product trafficking in MnSOD and underscore the utility of rational mutagenesis in accessing elusive mechanistic states.

Keywords: Manganese superoxide dismutase; Metalloenzyme; Proton-coupled electron transfer; Product transport; X-ray crystallography; Enzyme mechanism

1. Introduction:

Manganese superoxide dismutase (MnSOD, SOD2) is a metalloenzyme that catalyses the dismutation of mitochondrial superoxide radicals ($O_2^{\bullet-}$) into stable, diffusible products, hydrogen peroxide (H_2O_2) and molecular oxygen (O_2), thus acting as a first line of defense against oxidative stress. Consequently, dysfunctions in MnSOD expression or catalysis are linked to several diseases [1-2].

MnSOD operates through a highly efficient catalytic cycle, with a single Mn ion cycling between trivalent (oxidized, Mn^{3+}, pink) and divalent (reduced, Mn^{2+}, colorless) redox states while mediating two half-reactions that drive $O_2^{\bullet-}$ dismutation (Eqs. 1–2). In the first half-reaction, Mn^{3+} oxidizes $O_2^{\bullet-}$ to the first reaction product, O_2 (Eq. 1), and in the second, the Mn^{2+} reduces another $O_2^{\bullet-}$ radical to the final reaction product, H_2O_2, while regenerating the resting state catalytic Mn^{3+} (Eq. 2) [3-4].

$$Mn^{3+}\text{-WAT1}(OH^-) + O_2^{\bullet-} \leftrightarrow Mn^{2+}\text{-WAT1}(H_2O) + O_2 \quad (1)$$

$$Mn^{2+}\text{-WAT1}(H_2O) + O_2^{\bullet-} + 2H^+ \leftrightarrow Mn^{3+}\text{-WAT1}(OH^-) + H_2O_2 \quad (2)$$

Despite extensive structural characterization — 39 structures of human MnSOD and its variants are currently available in the Protein Data Bank (PDB) — all previous structures of H_2O_2-soaked MnSOD or its variants have only shown H_2O_2 binding at the active site or between the Tyr34-His30 gateway, with no evidence of any H_2O_2 binding sites along potential exit pathways [4-6]. This observation suggests that H_2O_2 release might be occurring too rapidly to be experimentally trapped by conventional methods, or that currently available H_2O_2-soaked MnSOD structures lack the high-resolution required to detect partially occupied H_2O_2 electron densities, or both. As a result, a critical gap remains in our mechanistic understanding of how substrate and reaction products traverse the ~10 Å deep and ~5 Å narrow active site cavity formed between adjacent subunits of the MnSOD enzyme. This is particularly important because MnSOD catalysis is typically limited by substrate and product diffusion, not by the intrinsic chemical transformation rates [7-8].

The goal of the present study is to address this gap by establishing the mechanism of H_2O_2 transport out of the MnSOD active site. To overcome

experimental challenges in capturing the highly rapid H_2O_2 transport process, we employed the kinetically slow and catalytically impaired Gln143AsnMnSOD variant. Gln143 is a second sphere residue that plays a critical role in the proton-coupled electron transfer (CPET) mechanism of native MnSODs. Specifically, in the first half-reaction, Gln143 donates a proton to the resting-state catalytic Mn^{3+}-bound solvent (WAT1-OH^-) to generate WAT1-H_2O (Eq. 1). Loss of the WAT1-OH^- negative charge destabilizes the positive charge of the oxidized metal (Mn^{3+}) center, priming it to lose an electron to generate the reduced state (Mn^{2+}). In the second half of the reaction (Eq. 2), Gln143 re-abstracts the proton from WAT1-H_2O, regenerating the WAT1-OH^- negative charge, which now primes the reduced metal to gain an electron to generate the oxidized state (Mn^{3+}). Thus, proton transfer between Gln143 and the metal-bound solvent is critical for the catalytic metals' redox cycling in MnSOD.

Through this reversible proton transfer event, Gln143 is directly coupled to the redox cycling of the catalytic metal in MnSOD that drives its catalysis. Substituting Gln143 with Asn preserves the overall side chain and backbone architecture but disrupts these critical proton transfer events in the Gln143Asn variant, as Asn143 is positioned too far from WAT1 to effectively participate in proton transfers [3]. Consequently, redox cycling of the catalytic Mn is slowed (Fig.1), evidenced by over 100-fold reductions in the corresponding kinetic rate constants, k_2 and k_4, relative to the wild-type MnSOD (Fig.1). This significantly impairs Gln43Asn MnSOD catalytic turnover (~13-fold decrease in K_{CAT} value relative to wild-type MnSOD). While this loss of catalytic efficiency compromises the overall function of Gln143Asn MnSOD, it offers a distinct experimental advantage for our study. The slowed turnover rate of Gln143Asn MnSOD allows for greater control of experimental design, cryo-trapping, and structural characterization of H_2O_2 molecules bound within and beyond the active site, all of which aid in the identification of the H_2O_2 exit route from the enzyme's active site.

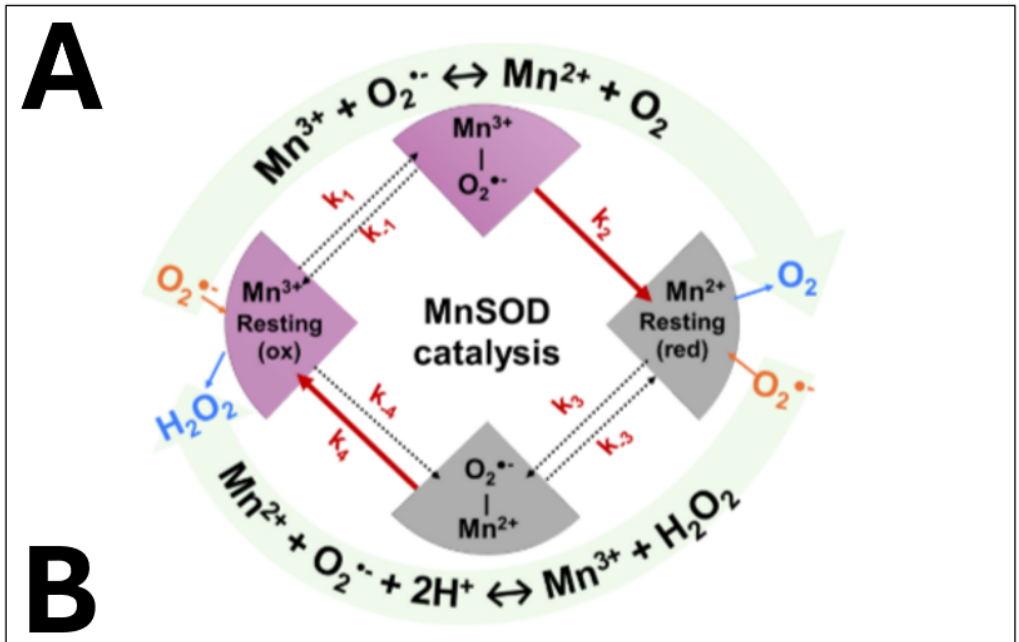

Equation	Rate constant	Gln143Asn	Wildtype
(1) $Mn^{3+} + O_2^{\bullet-} \leftrightarrow Mn^{2+} + O_2$	k_1 ($M^{-1}s^{-1}$)	2.0×10^9	2.0×10^9
	k_{-1} (s^{-1})	1.5×10^6	2.0×10^4
	k_2 (s^{-1})	600	8×10^4
	k_3 ($M^{-1}s^{-1}$)	2.0×10^9	2.0×10^9
	k_{-3}(s^{-1})	1.5×10^6	2.0×10^4
(2) $Mn^{2+} + O_2^{\bullet-} + 2H^+ \leftrightarrow Mn^{3+} + H_2O_2$	k_4 (s^{-1})	600	8×10^4
	k_{-4} ($M^{-1}s^{-1}$)	1×10^3	3×10^2

Figure 1. The kinetics of MnSOD catalysis. **(A)** MnSOD reaction scheme, with dashed black arrows indicating reaction rates that are similar, and solid red arrows indicating reaction steps that are slowed by the Gln143Asn mutation. **(B)** Kinetic parameters of human wild-type and Gln143Asn MnSOD enzymes. Data are from [8].

The results visualize how peroxide exits the Gln143Asn active site and how the gateway residue Tyr34 directs peroxide traffic. This solvent channel has previously been implicated as the entrance to the active site for water molecules and substrate analogues into the MnSOD active site [6]. Notably, this blocked gateway appears to be the principal bottleneck for product and possibly substrate diffusion, as evidenced by the striking accumulation of peroxides near it, forming a “traffic jam”, as they await release into the bulk solvent. Thus, combined with the previously established disruption of critical proton transfer reactions required for the successful redox cycling of Mn, this newly identified “blocked gateway” in the Gln143Asn variant renders H_2O_2 exit observable in “slow motion”, which offers rare experimental access to otherwise elusive catalytic states and transport pathways. Overall, we demonstrate that catalytically impaired enzyme variants, despite their near loss of function, can offer unique opportunities to capture elusive mechanistic steps, revealing otherwise inaccessible aspects of the catalytic cycle and advancing a more complete understanding of enzyme turnover.

2. Materials and Methods:

2.1. Expression, Purification & Crystallization of Gln143Asn MnSOD protein:

The Gln143Asn plasmid was ordered from GenScript and codon optimized for expression in *Escherichia coli. (E. coli)*. Following transformation of *E. coli* BL21(DE3) cells with the plasmid, a small culture was incubated at 37 °C and 225 rpm until visible turbidity was reached in Terrific Broth (TB) supplemented with 30 g/L of kanamycin. Next, 2 L of TB supplemented with 30 g/L of kanamycin and 16 mL of 100% glycerol was inoculated with ~5 mL of the small growth and incubated at 37 °C with vigorous shaking at 225 rpm until an OD_{600} of 0.8-1.0 was reached. A bolus of 8 mM $Mn^{2+}Cl_2$*4 H_20 and 1 mM isopropyl β-d-1-thiogalactopyranoside (IPTG) was then added, and the flasks were incubated at 37 °C and 140 rpm overnight. Induced cells were harvested by centrifugation using a Sorval Lynx 6000 with a Fiber Light F9-6x-1000 LEX rotor, operated at 4 °C and 8000 rpm for 40 minutes. The pellets were stored at –20 °C.

For Gln143Asn MnSOD protein purification, pellets were thawed at room temperature and thoroughly resuspended in Lysis buffer (10 mM $Mn^{2+}Cl_2$*4 H_20 and 10 mM MOPS pH 7.8), followed by filtration and removal of the insoluble fraction. Next, the soluble fraction was lysed with an EmulsiFlex-C3 at a pressure equal to or

greater than 20,000 psi for ~5 sample passes. The lysate was centrifuged at 4 °C and 8,000 rpm for 40 minutes, and the supernatant was transferred to a hot water bath at 55 °C for 1 hour. Then, the solute was centrifuged again, and the supernatant (containing the soluble proteins) was diluted using 25 mM MES pH 5.5 at a 1:2 protein to buffer ratio. The diluted protein was then loaded onto a HiPrep 16x10 CMFF cation exchange column using an ÄKTA Pure HPLC (GE Healthcare). The sample was buffer exchanged into 10 mM MES at pH 5.5 on the column, followed by protein elution from the resin with 10 mM MES at pH 6.5. Purification was confirmed by the presence of a single band corresponding to the correct molecular weight of 23 kDa on a 4-12% SDS PAGE gel stained with Coomassie blue.

Before crystallization, all pure fractions were pooled together, and buffer exchanged into 0.25 mM potassium phosphate (pH 7.8) using a 10 kDa concentrator (Millipore, Sigma Aldrich) and concentrated to ~23 mg/ml (~1 mM). 24-well hanging drop trays were set up with a 1:1 ratio of concentrated protein against reservoir solution containing 1.8 M potassium phosphate (pH 7.8) and incubated at room temperature. Gln143Asn MnSOD crystallized in the high-symmetry space group of $P6_122$, and the crystals grew to final sizes of ~ 100 µm long in a week. The crystal trays were hand-carried by flight to the Stanford Synchrotron Radiation Lightsource (SSRL) for data collection.

2.2. <u>X-ray crystallography data collection, processing, refinement, and validation:</u>

A single crystal of Gln143Asn MnSOD was exchanged into cryo-solution (2.5 M potassium phosphate, pH 7.8), then mounted with a 100 µm-sized cryo-loop (MiTeGen), followed by quick freezing in the cryo-steam at SSRL beamline 14-1. The mounted crystal was annealed by manually blocking the cryo-stream for 5 seconds. For H_2O_2 soaking, a 30% stock solution of H_2O_2 (Millipore Sigma) was diluted 100x and pipetted into the drop of mother liquor containing the single Gln143Asn crystal, to reach a final H_2O_2 concentration of 0.3% *in-crystallo*. The total soaking time was ~30 seconds at room temperature, followed by quick plunging into liquid nitrogen to cryo-trap the soaked H_2O_2 in the crystal, mounting, and annealing like the resting-state, resting state Gln143Asn MnSOD crystal. The process is schematized in Supplementary Fig. S1. X-ray crystallography data for both the resting-state and H_2O_2-treated Gln143Asn enzyme crystals were collected at 100 K,

at beamline 14-1 of SSRL, using a Dectris Pilatus 16M PAD detector and a controllable axial nitrogen cryo-stream (Oxford Cryosystems, Ltd.). Data collection parameters are summarized in Supplementary Table S1. Initial phases were obtained using the Phaser Molecular Replacement (Phaser-MR) package within the Phenix software suite [11-12] with the wild-type MnSOD structure (PDB ID: 7KLB) [3] serving as the phasing model.

Model building was performed with COOT [12] followed by iterative rounds of refinement cycles using Phenix_refine [13,16]**.** All refinement strategies were based on maximum likelihood-based target functions and included the refinement of i) individual atomic coordinates (in both reciprocal and real space), and ii) individual isotropic atomic displacement parameters (ADPs) for all atoms, with automatic weight optimisation. Only riding hydrogens were added to the models [14] and appropriate metal coordination restraints were generated using idealised geometries, with the ReadySet tool [16]. Gln143Asn, like the wild-type enzyme, crystallizes as a homodimer, with monomers A and B in the asymmetric unit, and crystallographic symmetry operations were applied to generate the physiological tetramer, using the PyMOL Molecular Graphics System (Schrodinger, LLC). Final model validations were performed using MolProbity [19]. Coordinate error estimates, calculated with Phenix_refine [13,16], are reported in Supplementary Table S1 as a measure of model precision. Coordinates and structure factors for the resting-state and H_2O_2-treated Gln143Asn MnSOD X-ray crystal structures have been deposited in the Protein Data Bank (PDB) under accession codes 9NR0 and 9NSJ, respectively.

2.3. Metal center-specific electrostatic surface generation:

To generate the solvent-excluded electrostatic surfaces of tetrameric MnSOD proteins that accurately reflect the electronic charge distribution, spin multiplicity, and redox potential of the active site Mn centres, we implemented a multistep protocol to account for electronic effects imparted by its primary coordination sphere (PCS) ligands [16] , schematized in Supplementary Fig. S2.

Step 1. Initial per-residue charges were assigned using the PDB2PQR [17] web service, hosted at poissonboltzmann.org. This generated PQR files containing i) atomic partial charges of all residues, computed using the AMBER force field [22-

24], and ii) protonation states of ionizable residues, based on pKa values predicted by PROPKA 3.0 at pH 7.0 [25-26].

Step 2. To determine the electronic properties of the Mn active site in specific redox and spin states, the protein structures were truncated to only retain the first-shell ligands coordinating the Mn ion, thereby preserving the key geometric and electronic features of the metal site. Density functional theory (DFT) calculations were performed on the isolated metal centers, using the high-spin sextet state for the divalent Mn ion in Gln143Asn enzyme [5], according to established protocols in [10, 27]. Single-atomic electrostatic potential (ESP) charges for the Mn ion and its direct ligands were derived using the Merz-Kollman scheme [18] and subsequently refined using the restrained electrostatic potential (RESP) methodology. As a benchmark, we applied the same DFT protocol to the five-coordinate, high-spin quintet resting-state of the wild-type Mn^{3+}SOD enzyme (PDB ID 5VF9) [10]. All DFT-calculated ESP charges are shown in Supplementary Fig. S3 and summarized in Supplementary Table S2.

Step 3. The ESP-refined metal charges were then integrated with the remainder of the tetrameric protein's PQR-derived charges to generate full electrostatic surface maps. They were computed using the Adaptive Poisson-Boltzmann Solver (APBS) Electrostatics [17] plugin within PyMOL, with ionic strengths set to 0.15 and -0.15M for positively and negatively charged species, respectively, following the established protocol in [4] .

2.4. Mn K-edge HERFD XANES data collection and analysis:

A solution of 3 mM Gln143Asn MnSOD (~70 mg ml^{-1}) in 25 mM potassium phosphate (pH 7.8) was treated with 280 mM (1% *w/v*) H_2O_2 to isolate the H_2O_2-bound state of the Gln143Asn variant. Mn K-edge HERFD-XANES spectra were recorded using a liquid He cryostat at 10 K, at beamline 15 − 2 of SSRL. The incident energy was tuned to the first derivative of an internal Mn foil at 6539 eV. X-ray irradiation was carefully monitored so that two subsequent scans of the same spot did not have photoreduction differences, and different spots along samples were scanned. When appropriate, aluminium foil was inserted into the beam path to attenuate the incident flux. For HERFD-XANES measurements, a Johann-type hard

X-ray spectrometer with six Mn analyser crystals were used with a liquid-nitrogen cooled Si (311) double crystal monochromator.

Experimental spectra were processed, visualized, and plotted using the Larch software package [29]. The post-edge regions were normalized, and pre-edge peak fittings were done using pseudo-Voigt functions. Pre-edge intensities were quantified as the integrated area under the fitted curves.

3. Results & Discussions:

3.1. Pathway of H_2O_2 exit out of the human Gln143Asn MnSOD active site.

We report two high-resolution X-ray crystal structures of the Gln143Asn MnSOD enzyme: (i) a 1.33 Å structure of the H_2O_2-treated form (PDB ID: 2NR0) and (ii) a 1.55 Å structure of the resting-state form (PDB ID: 2NSJ). Most published H_2O_2-bound MnSOD structures have reported either fully or partially occupied H_2O_2 molecules directed ligated to the catalytic Mn within the active site [30-31]. A recent neutron structure of the Trp161Phe MnSOD variant further revealed a second peroxide binding site, PEO, positioned between the solvent channel gateway residues, Tyr34 and His30 [5]. In this present study, we report, a striking accumulation of cryo-trapped H_2O_2 molecules, moving out of the active site of the human Gln143Asn enzyme and into the bulk solvent, via the solvent funnel, and flowing between MnSOD gateway residues, Tyr34 and His30 (Fig. 2). These H_2O_2 molecules appear to be sequentially positioned along a continuous trajectory, extending from the mouth of the gateway, forming what be best described as a “traffic jam” of peroxides exiting the catalytically impaired active site of the Gln143Asn variant (Fig. 2A, blue arrows show direction of peroxide diffusion out of the MnSOD solvent funnel). Such an unprecedented number of H_2O_2 molecules has not been trapped in any MnSOD structure before. These findings provide strong validation for our chosen experimental strategy, which leverages the slowed catalysis of the Gln143Asn variant to reveal the H_2O_2 exit pathway in human MnSOD.

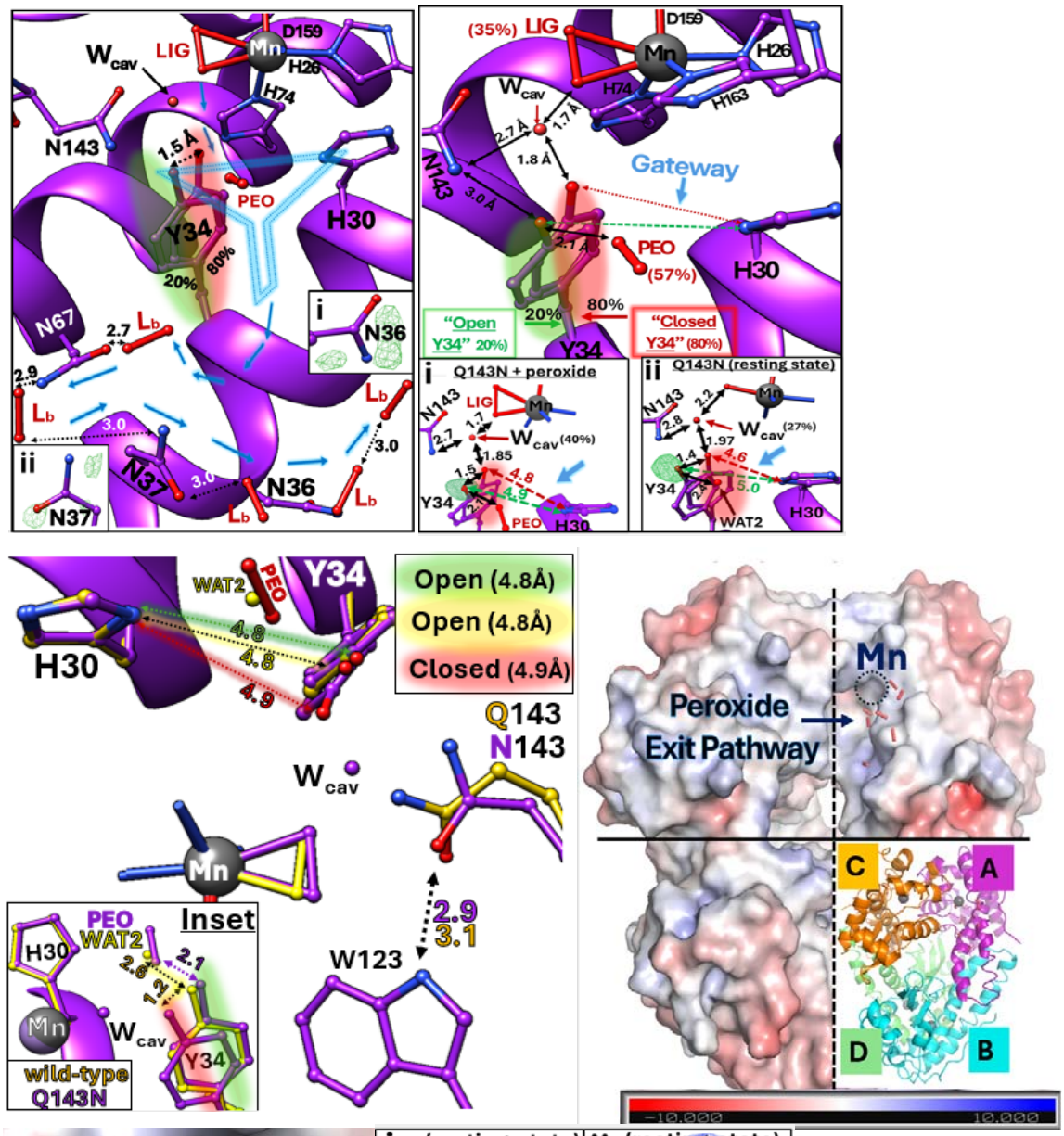

Wcav
LIG
Mn
D159
H26
H74
N143
1.5 Å
PEO
Y34
H30
20%
80%
N67
2.7
Lb
2.9
3.0
N37
N36
i
ii
(35%) LIG
H163
Gateway
2.7 Å
1.7 Å
1.8 Å
3.0 Å
2.1 Å
PEO
(57%)
"Open Y34" 20%)
"Closed Y34" (80%)
Q143N + peroxide
Q143N (resting state)
Wcav (40%)
Wcav (27%)
WAT2
Open (4.8Å)
Open (4.8Å)
Closed (4.9Å)
4.8
4.9
Q143
N143
2.9
3.1
W123
Inset
wild-type
Q143N
Peroxide
Exit Pathway
C
A
D
B
-10.000
10.000

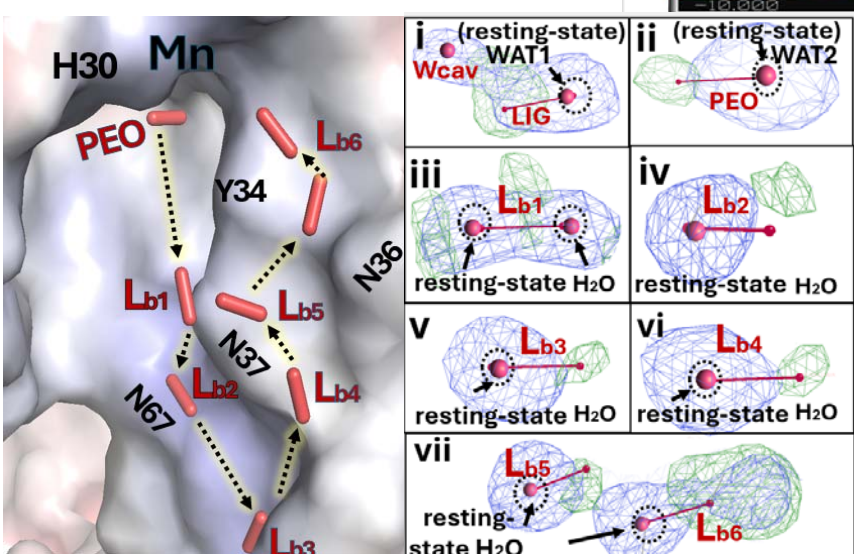

H30
Mn
PEO
Y34
Lb6
Lb1
Lb5
N36
N37
N67
Lb2
Lb4
Lb3
i (resting-state)
WAT1
Wcav
LIG
ii (resting-state)
WAT2
PEO
iii
Lb1
resting-state H2O
iv
Lb2
resting-state H2O
v
Lb3
resting-state H2O
vi
Lb4
resting-state H2O
vii
Lb5
resting-state H2O
Lb6

D159

Figure 2. The structure of peroxide-bound Gln143Asn MnSOD. **(A)** Blue arrows indicate LIG exit route from Gln143Asn MSOD active site via the solvent gateway, aka the MnSOD solvent funnel (depicted as a cartoon blue funnel flanked by gateway residues Tyr34 and His30). Interactions between Asn67, Asn37, and Asn36, and the trailing H_2O_2 molecules exiting into the bulk solvent (named L_b for L_{bulk}) are shown by dashed arrows. **(Insets i-ii)** show the difference electron densities for the mobile Asn residues as green mesh, contoured at 3.0σ. **(B)** H_2O_2 bound near the Tyr34 "closed" conformation is labelled PEO, to be consistent with to literature. **Insets i-ii** show gateway constriction caused by the 80% populated, "closed" Tyr34 conformation (shaded red) in the H_2O_2 -treated, and resting-states of Gln143Asn MnSOD respectively, with gateway opening marked by a single solid blue arrow. **(C)** Superposition of H_2O_2 -bound Gln143Asn (purple) with wild-type MnSOD (yellow, PDB 8VJ5) shows that Tyr34 exclusively samples the "open" conformation in the wild-type, which is sampled only ~20% of the time in the Gln143Asn variant. **Inset** shows close-up view of the unobstructed solvent gateway opening in the wild-type MnSOD, corresponding to the minority sampled "open" Tyr34 conformation in the Gln143Asn variant. **(D)** H_2O_2 exit pathway in Gln143Asn MnSOD, overlaid on the electrostatic surface of the tetramer. The active site of chain A is circled, and all L_b peroxides are shown as red sticks. Dimeric and tetrameric interfaces are marked by dashed and solid black lines, respectively**.** **Inset:** Ribbon diagram of the tetrameric Gln143Asn MnSOD, with Mn ions shown as grey spheres. **(E)** Close-up of L_b peroxides exiting through the Tyr34-His30 gateway. **Insets i–vii** show the difference electron densities (green mesh, contoured at 3.0σ) resulting from modeling fully occupied waters (shown as red spheres marked by dashed black circles) in place of the fully occupied individual L_b peroxides (shown here as thin red wires) in the H_2O_2-treated Gln143Asn structure. All 2Fo-Fc and Fo-Fc electron densities are shown as blue and green mesh (contoured at 1.0 and 3.0σ, respectively).

Moreover, we have identified several asparagine residues, namely Asn67, Asn37, and Asn36, lining this exit-pathway, which sample alternate conformations to coordinate movement of H_2O_2 towards the solvent-exposed exterior of the enzyme (Fig. 2A inset i-iii). We shall refer to this pathway as the H_2O_2 exit pathway.

Our X-ray crystallography data reveal that H_2O_2 diffusion from the Gln143Asn active site, via the H_2O_2 exit-pathway, is directed by the well-characterised MnSOD gateway residue, Tyr34 (Fig. 2A-B). Notably, we observe a significant positive difference (F_o-F_c) electron density around the phenol ring of Tyr34 at 3.5 σ (Fig. 2B, inset i), along with elevated B-factors relative to neighboring residues, all of which suggest that Tyr34 is undergoing a dynamic transition in the Gln143Asn variant. In this variant, Tyr34 undergoes conformational rearrangement, which has significant mechanistic implications for the release of H_2O_2 from its active site Mn^{2+} -bound (LIG) position [5, 30]. Similar Tyr34 conformational dynamics are also observed in the resting state of the Gln143Asn enzyme (Fig. 2B, inset ii). Therefore, this dynamic behavior of Tyr34 is a unique and intrinsic property of this specific MnSOD variant, irrespective of H_2O_2 soaking. It can be attributed to the Gln143Asn substitution, which introduces a localised cavity adjacent to the active site, that now accommodates either an extra cavity water (named W_{cav}), or a novel "closed" conformation of Tyr34, which is the dominant conformation of Tyr34 in this variant (Fig. 2B-E). In contrast, this occlusive Tyr34 conformation is sterically restricted in the H_2O_2-bound and resting-state of the wild-type enzyme, which exclusively supports the "open" state (Fig. 2C, Supplementary Fig.S4).

We propose that in the Gln143Asn MnSOD variant, the inherently flexible Tyr34 adopts a "closed" conformation ~80% of the time in both resting-state and following H_2O_2-treatment. This occlusive Tyr34 conformation narrows the gateway between Tyr34 and His30, restricting solvent access and impeding H_2O_2 (LIG) diffusion out of the Mn coordination sphere. Fig. 2 B-C shows the two primary Tyr34 conformations observed in the Gln143Asn MnSOD enzyme: the dominant "closed" (red) state (80% occupancy), and the minor "open" (green) state, with the mouth of the solvent gateway marked by a solid blue arrow. When Tyr34 shifts to the "open" (green) state, LIG escapes its side-on Mn-bound (LIG) position, briefly occupying a second H_2O_2 binding site (PEO), at the gateway mouth (Fig. 2B-C). This occluded exit-pathway, enforced by the "closed" (red) state of the Tyr34 residue, acts as the principal bottleneck for H_2O_2 release in this unique MnSOD variant.

Interestingly, when waters are modelled at full occupancy, at positions corresponding to bulk solvent exposed H_2O_2 positions (named L_b for Lig_{bulk}), we observe a significant difference electron (Fo-Fc) density at 3 σ (Fig.2E, insets i-vii).

This strongly supports the presence of electron density consistent with two oxygen atoms, as expected for a H_2O_2 molecule, rather than single oxygen-containing water. Moreover, a superposition with the resting state Gln143Asn MnSOD control structure reveals that these positions are otherwise occupied by water molecules in the absence of H_2O_2 soaking, confirming that the observed H_2O_2 molecules originate from our soaking experiment rather than X-ray induced radiolysis (Supplementary Fig.S5).

Overall, our results show that, metaphorically, Tyr34 functions like a “broke” traffic light in the Gln143Asn MnSOD, stuck on “red” (closed) most of the time, delaying H_2O_2 exit. Supported by omit electron density maps and B-factor analyses, we propose the following sequence for H_2O_2 release: (1) In the majority-populated “closed” (red) conformation, Tyr34 blocks the solvent gateway, preventing H_2O_2 (LIG) from dissociating from Mn^{2+}. (2) When Tyr34 samples the “open” (green) conformation (that is exclusively observed in wild-type MnSOD), the gateway widens, allowing LIG to dissociate from Mn^{2+} and exit the metal coordination sphere. (3) H_2O_2 then transiently binds at the PEO site near the gateway mouth before diffusing into bulk solvent. The rare shift to the “open” (green) state makes H_2O_2 release a bottleneck event in the Gln143Asn MnSOD, forcing accumulation near the mouth of the solvent gateway like traffic at a chronically red light.

3.2. Peroxide treatment induced side-on H_2O_2 binding: Impact on Mn redox and electronic structure in the Gln143Asn MnSOD.

H_2O_2 treatment does not significantly alter the overall architecture of the active site of Gln143Asn MnSOD, except for the displacement of the fully occupied Mn-bound solvent (WAT1) by a partially occupied (~35%) H_2O_2 molecule (LIG) opposite His26 (Fig. 3A). Superposition with H_2O_2-treated human and *E.coli* wild-type MnSOD enzymes shows that in the Gln143Asn variant (Fig. 3B, purple), H_2O_2 binds the active site LIG position in a configuration very similar to the previously observed side-on binding mode in the human wild-type enzyme (Fig. 3B, yellow, PDB 8VJ5), rather than end-on, as seen in the *E.coli* wild-type MnSOD (Fig. 3B, orange, PDB 3K9S). DFT calculations predict no significant change in the charge or spin state of the catalytic Mn^{2+} upon H_2O_2 treatment. However, certain trends emerge (Supplementary Fig. S3 and Table S2): (i) Charges of both His26, and His74 switch signs, going from positive to negative (and closer to the wild-type resting-state

values), (ii) Asp159 is less negatively charged in the resting-state of Gln143Asn, compared to wild-type, but becomes more negative, with peroxide addition, and (iii) His163 flips from negative to positive charge when comparing the wild-type to the variant, indicating potential protonation state change. However, these conclusions remain to be experimentally validated. It is important to note that our DFT models treat LIG as a di-oxygen species rather than hydrogen peroxide(H_2O_2), as its protonation state cannot be accurately determined from X-ray data alone, even at high resolutions, without neutrons. This is particularly relevant considering recent neutron diffraction studies of H_2O_2-soaked Trp161Phe (Fig. 3C, cyan, PDB 8VHW), and Tyr34Phe (Fig. 3C, red, PDB 9BVY) Mn^{2+}SODs, both of which stabilize a singly protonated di-oxygen species, hydroperoxyl anion ($^{-}$OOH), following H_2O_2 -induced metal reduction (Fig. 3C).

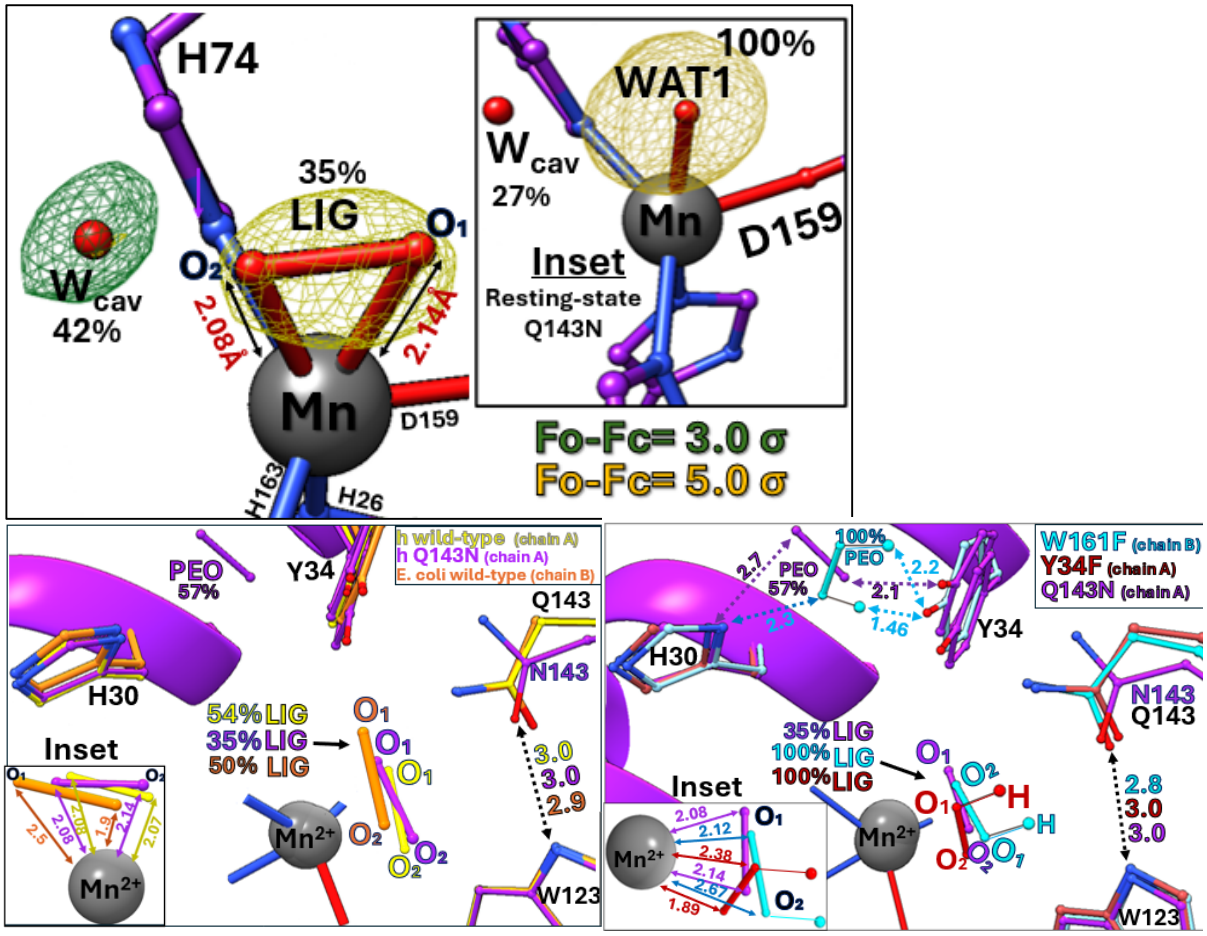

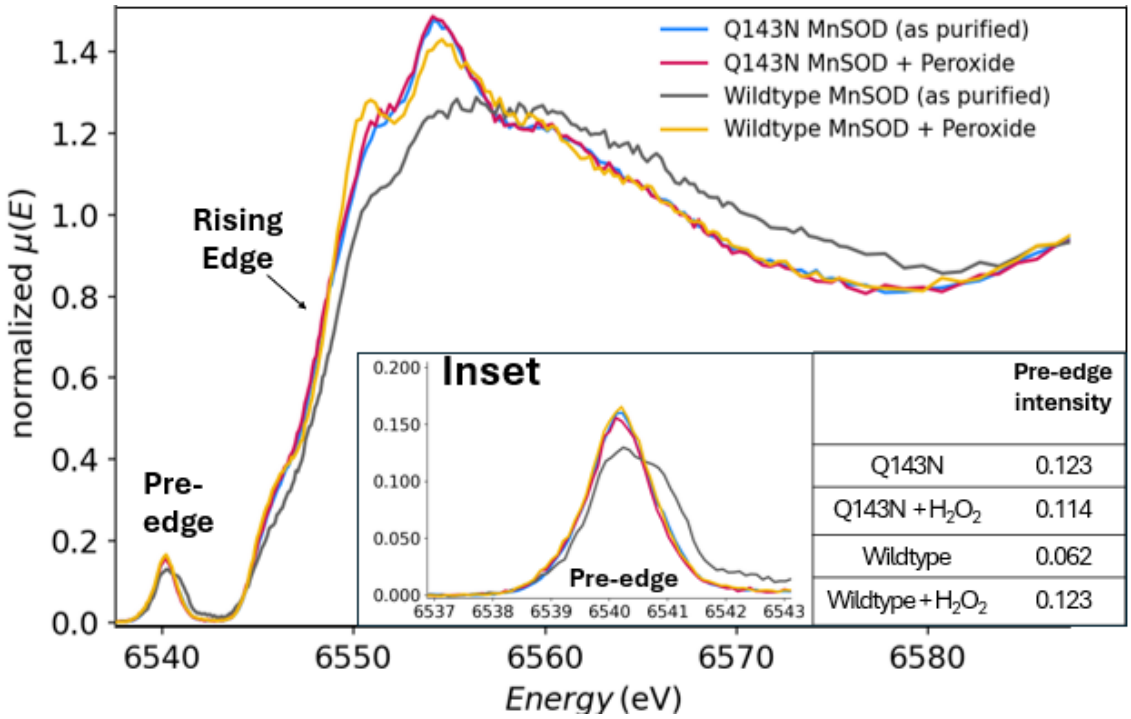

	Pre-edge intensity
Q143N	0.123
Q143N + H_2O_2	0.114
Wildtype	0.062
Wildtype + H_2O_2	0.123

Figure. 3: Peroxide binding modes and associated Mn redox and electronic states in MnSOD. (**A**) Active site of H_2O_2-treated Gln143Asn (purple, PDB 9NSJ) with **inset** showing the resting-state of Gln143Asn MnSOD (purple, PDB 9NR0). Omit electron densities for WAT1, LIG, and W_{cav} are displayed over their modelled positions. Superposition of the H_2O_2-treated Gln143Asn (purple) with **(B)** human (yellow) and *E. coli* (orange) H_2O_2-bound wild-type MnSODs and **(C)** Trp161Phe (cyan) and Tyr34Phe (red) MnSODs reveals subtle differences in peroxide binding modes in these variants. **(D)** Normalized Mn K-edge HERFD-XANES spectra of wild-type and Gln143Asn MnSOD enzymes, both in resting and H_2O_2-soaked forms. **Inset** shows a magnified view of the pre-edge region (6537–6543 eV), along with their individual pre-edge intensities.

Additionally, a second-shell H_2O_2 binding site, referred to as PEO, is observed between gateway residues Tyr34 and His30 in both chains of the H_2O_2-treated Gln143Asn MnSOD (Fig. 3B–C, purple). This site corresponds to a similar H_2O_2 binding site reported in the H_2O_2-soaked neutron structure of Trp161Phe MnSOD, where it was observed only in chain B and at full occupancy (Fig. 3C, cyan; PDB 8VHW). Superposition of the two H_2O_2-bound MnSOD variants reveals that peroxide binds at the PEO site at a slightly different angle in the Gln143Asn variant.

To monitor changes in the oxidation state and coordination geometry of the catalytic Mn in the Gln143Asn variant upon H_2O_2 exposure, we compared the Mn K-edge High-Energy-Resonance Fluorescence-Detected X-ray Absorption Near-Edge Spectra (HERFD-XANES) of the purified enzyme, before and after H_2O_2 treatment, following protocols established in [5, 30]. Overall, we observe no detectable shift in either rising edge or pre-edge features (Fig. 3D, blue and red), indicating no alteration in the redox state or coordination geometry of the catalytic Mn after H_2O_2 treatment in the Gln143Asn enzyme.

Notably, the spectral features of both Gln143Asn samples closely resemble those of the H_2O_2-treated wild-type MnSOD (Fig. 3D, yellow), which has been previously established to contain the reduced Mn^{2+} ion in its active site [9]. The pre-edge intensities of both Gln143Asn samples are comparable to each other and the H_2O_2-treated wild-type enzyme, indicating highly similar metal centers across all three conditions. In contrast, the spectrum of the resting-state wild-type MnSOD

(Fig. 3D, dark grey) shows a clear shift of both rising and pre-edge features toward higher energies, consistent with the established presence of an oxidized Mn^{3+} metal in the resting wild-type MnSOD.

Thus, we conclude that both the Gln143Asn samples, as well as the H_2O_2-treated wild-type enzyme, exhibit a one-electron reduction in the oxidation state of their catalytic metal centers. H_2O_2 treatment does not alter the redox state or coordination geometry of the catalytic Mn in the Gln143Asn MnSOD variant, in contrast to most osther MnSOD variants [30, 5, 9]. Taken together, these findings indicate that the Gln143Asn substitution fundamentally and irreversibly alters the redox properties of the MnSOD active site, exclusively stabilizing the reduced Mn^{2+} state under both resting and H_2O_2-bound conditions. This loss of redox flexibility occurs at the expense of catalytic turnover and distinguishes Gln143Asn from all other spectrally characterized human MnSOD variants to date.

4. Conclusions:

While the overall structure of Gln143Asn MnSOD looks very similar to the wild-type enzyme, a closer look reveals some subtle differences with the wild-type MnSOD, irrespective of H_2O_2 soaking. (i) The Gln143 to Asn substitution induced cavity serves as a binding site for an “extra” solvent, W_{cav} (Fig. 2 and Supplementary Fig.S4A), which generates new hydrogen bonds within the Gln143Asn active site. It could be speculated that these additional hydrogen bonds in Gln134Asn MnSOD potentially contribute to its ~1.8°C higher thermal stability relative to the wild-type enzyme [32]. (ii) presence of a partially-bound, sixth ligand (referred to as L_{SIX}) to the reduced metal in the resting-state and H_2O_2-treated Gln143Asn MnSOD (Supplementary Fig.S6).

We also present structural evidence of a defined exit pathway for product H_2O_2 in human MnSOD, using the catalytically impaired Gln143Asn variant. This pathway enables direct diffusion of H_2O_2 from its Mn^{2+} side-on bound position (LIG), through the active site gateway to the solvent channel, and into the bulk solvent. Notably, Tyr34 has conformational flexibility in the cavity formed by the Gln143 to Asn substitution in this unique variant, and in doing so, essentially narrows the mouth of the gateway in its majority populated “closed” conformation, which slows down the exit of H_2O_2 from the metals’ primary coordination sphere.

In fact, this blocked gateway appears to be the principal bottleneck for product and possibly substrate diffusion, as evidenced by the striking accumulation of peroxides near it, forming a “traffic jam”, as they await release into the bulk solvent. Thus, combined with the previously established disruption of critical proton transfer reactions required for the successful redox cycling of Mn, this newly identified “blocked gateway” in the Gln143Asn variant renders H_2O_2 exit observable in “slow motion”, which offers rare experimental access to otherwise elusive catalytic states and transport pathways. Thus, the Gln143Asn MnSOD variant essentially enables a “slow-motion” version of MnSOD catalysis, offering a rare window into product egress events that are otherwise too rapid to capture.

Collectively, these structural insights reveal a previously uncharacterized role for Tyr34 in directing peroxide exit from MnSOD and underscore the dynamic role of second-sphere residues in fine-tuning the catalytic function of metalloenzymes. This newly visualized pathway for H_2O_2 diffusion out of the MnSOD active site offers new insight into how product clearance is orchestrated in this essential mitochondrial antioxidant enzyme. Remarkably, these insights were achieved using a catalytically impaired MnSOD variant, which displays markedly reduced turnover relative to the wild-type enzyme. While the Gln143 to Asn substitution compromises activity, it simultaneously stabilizes fleeting catalytic intermediates and allows for the cryo-trapping and visualization of structural conformations that would be too elusive to capture in the wild-type enzyme.

Overall, our study demonstrates that catalytically impaired enzyme variants, despite their near loss of function, can offer unique opportunities to capture elusive mechanistic steps and advance a more complete understanding of enzyme turnover, as well as the powerful synergy of rational mutagenesis with high-resolution X-ray crystallography and spectroscopy methods in dissecting enzymatic reaction mechanisms.

5. Data Availability:

Coordinates and structure factors for X-ray crystallographic data generated in this study have been deposited in the Protein Data Bank under the following accession codes (**9NR0** and **9NSJ**). All relevant data supporting the key findings of this study are available within this article and its Supplementary Information. Additional raw

diffraction images and X-ray spectroscopy data, and models are available from the corresponding author upon request.

6. CRediT authorship contribution statement:

Medhanjali Dasgupta: Conceptualization, Methodology, Software, Validation, Formal analysis, Data curation, Writing – original draft, Writing – review & editing. **Gloria E. O. Borgstahl:** Conceptualization, Methodology, Investigation, Funding acquisition, Project administration, Supervision, Writing – review & editing. **Thomas Kroll:** Methodology, Software, Supervision, Formal analysis. **Katie Slobodnik, Erika A Cone and Jahaun Azadmanesh:** Visualization, Investigation, Writing – review & editing.

7. Declaration of competing interest:

The authors declare no competing financial or personal relationships that could appear to have influenced the work reported in this manuscript.

8. Acknowledgements:

This research was funded by the NIGMS grant R01-GM145647. The UNMC Structural Biology Core Facility received support from the Fred and Pamela Buffett NCI Cancer Center Support Grant (P30CA036727). The use of the Stanford Synchrotron Radiation Lightsource (SSRL) at SLAC National Accelerator Laboratory, is supported by the US Department of Energy (DOE), Office of Science, Office of Basic Energy Sciences under Contract No. DE-AC02-76SF00515. The SSRL Structural Molecular Biology Program is funded by the DOE Office of Biological and Environmental Research and the NIH National Institute of General Medical Sciences (P30GM133894). The views expressed in this publication are those of the authors and do not necessarily reflect the official positions of NIGMS, NIH or the DOE.

References:

[1] M. Liu, X. Sun, B. Chen, R. Dai, Z. Xi, H. Xu, 2022. Insights into Manganese Superoxide Dismutase and Human Diseases. International Journal of Molecular Sciences. 23, 15893. https://doi.org/10.3390/ijms232415893

[2] J. C. Mayo, R. M. Sainz, I. Quiros-Gonzalez, 2018. MnSOD/SOD2 in Cancer: The Story of a Double Agent. Reactive Oxygen Species. 5, 86–106

[3] J. Azadmanesh, W. E. Lutz, L. Coates, K. L. Weiss, G. E. O. Borgstahl, 2021. Direct detection of coupled proton and electron transfers in human manganese superoxide dismutase. Nat Commun. 12, 2079. https://doi.org/10.1038/s41467-021-22290-1

[4] J. Azadmanesh, S. R. Trickel, G. E. O. Borgstahl, 2017. Substrate-analog binding and electrostatic surfaces of human manganese superoxide dismutase. Journal of Structural Biology. 199, 68–75. https://doi.org/10.1016/j.jsb.2017.04.011

[5] J. Azadmanesh, K. Slobodnik, L. R. Struble, W. E. Lutz, L. Coates, K. L. Weiss, D. A. A. Myles, T. Kroll, G. E. O. Borgstahl, 2024. Revealing the atomic and electronic mechanism of human manganese superoxide dismutase product inhibition. Nat Commun. 15, 5973. https://doi.org/10.1038/s41467-024-50260-w

[6] J. Azadmanesh, K. Slobodnik, L. R. Struble, J. J. Lovelace, E. A. Cone, M. Dasgupta, W. E. Lutz, S. Kumar, A. Natarajan, L. Coates, K. L. Weiss, D. A. A. Myles, T. Kroll, G. E. O. Borgstahl, 2025. The role of Tyr34 in proton coupled electron transfer and product inhibition of manganese superoxide dismutase. Nat Commun. 16, 1887. https://doi.org/10.1038/s41467-025-57180-3

[7] J. Porta, A. Vahedi-Faridi, G. E. O. Borgstahl, 2010. Structural Analysis of Peroxide-Soaked MnSOD Crystals Reveals Side-On Binding of Peroxide to Active-Site Manganese. Journal of Molecular Biology. 399, 377–384. https://doi.org/10.1016/j.jmb.2010.04.031

[8] J.-L. Hsu, Y. Hsieh, C. Tu, D. O'Connor, H. S. Nick, D. N. Silverman, 1996. Catalytic Properties of Human Manganese Superoxide Dismutase *. Journal of Biological Chemistry. 271, 17687–17691. https://doi.org/10.1074/jbc.271.30.17687

[9] W. H. Bannister, J. V. Bannister, 1987. Factor Analysis of the Activities of Superoxide Dismutase, Catalase and Glutathione Peroxidase in Normal Tissues and Neoplastic Cell Lines. Free Radical Research Communications. 4, 1–13. https://doi.org/10.3109/10715768709088082

[10] P. D. Adams, P. V. Afonine, G. Bunkóczi, V. B. Chen, I. W. Davis, N. Echols, J. J. Headd, L.-W. Hung, G. J. Kapral, R. W. Grosse-Kunstleve, A. J. McCoy, N. W. Moriarty, R. Oeffner, R. J. Read, D. C. Richardson, J. S. Richardson, T. C. Terwilliger, P. H. Zwart, 2010. PHENIX: a comprehensive Python-based system for macromolecular structure solution. Acta Crystallogr D Biol Crystallogr. 66, 213–221. https://doi.org/10.1107/S0907444909052925

[11] A. J. McCoy, 2006. Solving structures of protein complexes by molecular replacement with Phaser. Acta Crystallogr D Biol Crystallogr. 63, 32–41. https://doi.org/10.1107/S0907444906045975

[12] P. Emsley, K. Cowtan, 2004. Coot: model-building tools for molecular graphics. Acta Crystallogr D Biol Crystallogr. 60, 2126–2132. https://doi.org/10.1107/S0907444904019158

[13] D. Liebschner, P. V. Afonine, M. L. Baker, G. Bunkóczi, V. B. Chen, T. I. Croll, B. Hintze, L.-W. Hung, S. Jain, A. J. McCoy, N. W. Moriarty, R. D. Oeffner, B. K. Poon, M. G. Prisant, R. J. Read, J. S. Richardson, D. C. Richardson, M. D. Sammito, O. V. Sobolev, D. H. Stockwell, T. C. Terwilliger, A. G. Urzhumtsev, L. L.

Videau, C. J. Williams, P. D. Adams, 2019. Macromolecular structure determination using X-rays, neutrons and electrons: recent developments in Phenix. Acta Crystallogr D Struct Biol. 75, 861–877. https://doi.org/10.1107/S2059798319011471

[14] D. Liebschner, P. V. Afonine, A. G. Urzhumtsev, P. D. Adams, 2020. Implementation of the riding hydrogen model in CCTBX to support the next generation of X-ray and neutron joint refinement in Phenix. Methods in Enzymology. 634, 177–199. https://doi.org/10.1016/bs.mie.2020.01.007

[15] C. J. Williams, J. J. Headd, N. W. Moriarty, M. G. Prisant, L. L. Videau, L. N. Deis, V. Verma, D. A. Keedy, B. J. Hintze, V. B. Chen, S. Jain, S. M. Lewis, W. B. Arendall, J. Snoeyink, P. D. Adams, S. C. Lovell, J. S. Richardson, D. C. Richardson, 2018. MolProbity: More and better reference data for improved all-atom structure validation. Protein Sci. 27, 293–315. https://doi.org/10.1002/pro.3330

[16] C. Van Stappen, H. Dai, A. Jose, S. Tian, E. I. Solomon, Y. Lu, 2023. Primary and Secondary Coordination Sphere Effects on the Structure and Function of S-Nitrosylating Azurin. J Am Chem Soc. 145, 20610–20623. https://doi.org/10.1021/jacs.3c07399

[17] E. Jurrus, D. Engel, K. Star, K. Monson, J. Brandi, L. E. Felberg, D. H. Brookes, L. Wilson, J. Chen, K. Liles, M. Chun, P. Li, D. W. Gohara, T. Dolinsky, R. Konecny, D. R. Koes, J. E. Nielsen, T. Head-Gordon, W. Geng, R. Krasny, G.-W. Wei, M. J. Holst, J. A. McCammon, N. A. Baker, 2018. Improvements to the APBS biomolecular solvation software suite. Protein Science. 27, 112–128. https://doi.org/10.1002/pro.3280

[18] W. D. Cornell, P. Cieplak, C. I. Bayly, I. R. Gould, K. M. Merz, D. M. Ferguson, D. C. Spellmeyer, T. Fox, J. W. Caldwell, P. A. Kollman, 2002. A Second Generation Force Field for the Simulation of Proteins, Nucleic Acids, and Organic Molecules. ACS Publications. https://doi.org/10.1021/ja00124a002

[19] D. A. CASE, T. E. CHEATHAM, T. DARDEN, H. GOHLKE, R. LUO, K. M. MERZ, A. ONUFRIEV, C. SIMMERLING, B. WANG, R. J. WOODS, 2005. The Amber Biomolecular Simulation Programs. J Comput Chem. 26, 1668–1688. https://doi.org/10.1002/jcc.20290

[20] S. J. Weiner, P. A. Kollman, D. A. Case, U. C. Singh, C. Ghio, G. Alagona, S. Profeta, P. Weiner, 2002. A new force field for molecular mechanical simulation of nucleic acids and proteins. ACS Publications. https://doi.org/10.1021/ja00315a051

[21] M. H. M. Olsson, C. R. Søndergaard, M. Rostkowski, J. H. Jensen, 2011. PROPKA3: Consistent Treatment of Internal and Surface Residues in Empirical pKa Predictions. J. Chem. Theory Comput. 7, 525–537. https://doi.org/10.1021/ct100578z

[22] C. R. Søndergaard, M. H. M. Olsson, M. Rostkowski, J. H. Jensen, 2011. Improved Treatment of Ligands and Coupling Effects in Empirical Calculation and Rationalization of pKa Values. J. Chem. Theory Comput. 7, 2284–2295. https://doi.org/10.1021/ct200133y

[23] R. P. P. Neves, S. F. Sousa, P. A. Fernandes, M. J. Ramos, 2013. Parameters for Molecular Dynamics Simulations of Manganese-Containing Metalloproteins. J. Chem. Theory Comput. 9, 2718–2732. https://doi.org/10.1021/ct400055v

[24] M. Newville, 2013. Larch: An Analysis Package for XAFS and Related Spectroscopies. J. Phys.: Conf. Ser. 430, 012007. https://doi.org/10.1088/1742-6596/430/1/012007

[25] J. Azadmanesh, K. Slobodnik, L. R. Struble, W. E. Lutz, L. Coates, K. L. Weiss, D. A. A. Myles, T. Kroll, G. E. O. Borgstahl, 2024. Revealing the atomic and electronic mechanism of human manganese superoxide dismutase product inhibition. Nat Commun. 15, 5973. https://doi.org/10.1038/s41467-024-50260-w

[26] J. Azadmanesh, K. Slobodnik, L. R. Struble, E. A. Cone, M. Dasgupta, W. E. Lutz, S. Kumar, A. Natarajan, L. Coates, K. L. Weiss, D. A. A. Myles, T. Kroll, G. E. O. Borgstahl, 2024. The role of Tyr34 in proton-coupled electron transfer of human manganese superoxide dismutase, 2024.05.29.596464. https://doi.org/10.1101/2024.05.29.596464

[27] Y. Hsieh, Y. Guan, C. Tu, P. J. Bratt, A. Angerhofer, J. R. Lepock, M. J. Hickey, J. A. Tainer, H. S. Nick, D. N. Silverman, 1998. Probing the Active Site of Human Manganese Superoxide Dismutase: The Role of Glutamine 143,. Biochemistry. 37, 4731–4739. https://doi.org/10.1021/bi972395d

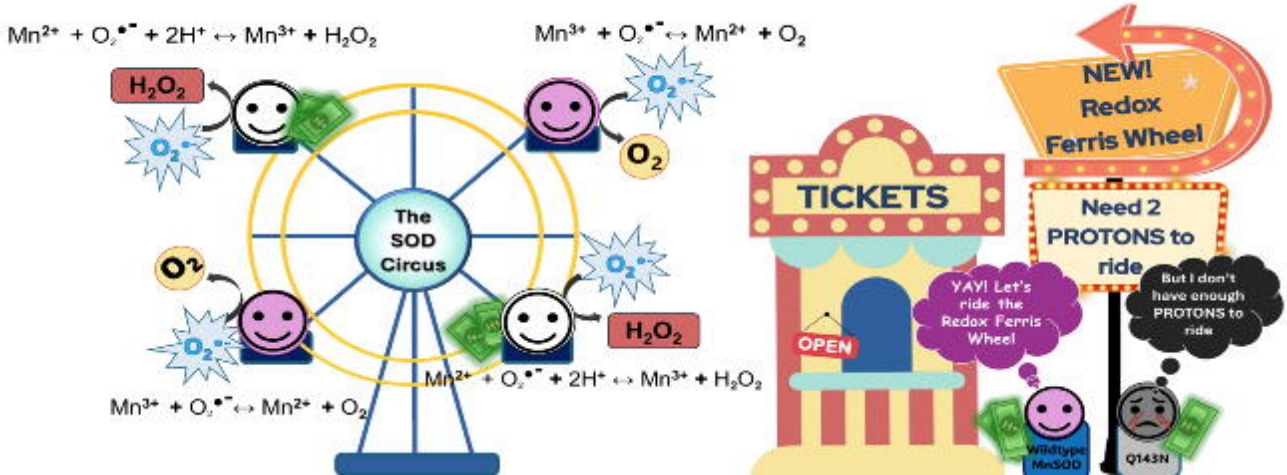
$Mn^{2+} + O_2^{\bullet -} + 2H^+ \leftrightarrow Mn^{3+} + H_2O_2$
$Mn^{3+} + O_2^{\bullet -} \leftrightarrow Mn^{2+} + O_2$
H_2O_2
$O_2^{\bullet -}$
O_2
The SOD Circus
$Mn^{2+} + O_2^{\bullet -} + 2H^+ \leftrightarrow Mn^{3+} + H_2O_2$
$Mn^{3+} + O_2^{\bullet -} \leftrightarrow Mn^{2+} + O_2$
NEW! Redox Ferris Wheel
TICKETS
OPEN
Need 2 PROTONS to ride
YAY! Let's ride the Redox Ferris Wheel
But I don't have enough PROTONS to ride
Wildtype MnSOD
Q143N

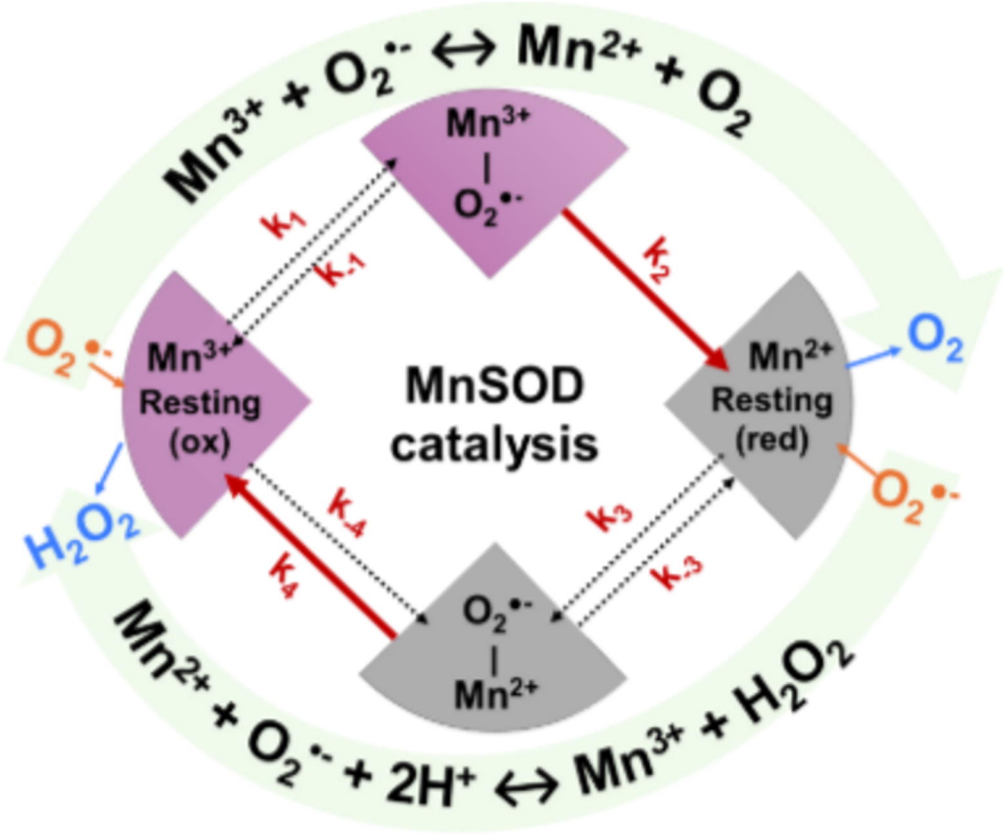

Equation	Rate constant	Gln143Asn	Wildtype
(1) $Mn^{3+} + O_2^{\bullet-} \leftrightarrow Mn^{2+} + O_2$	k_1 ($M^{-1}s^{-1}$)	2.0×10^9	2.0×10^9
	k_{-1} (s^{-1})	1.5×10^6	2.0×10^4
	k_2 (s^{-1})	600	8×10^4
	k_3 ($M^{-1}s^{-1}$)	2.0×10^9	2.0×10^9
	k_{-3}(s^{-1})	1.5×10^6	2.0×10^4
(2) $Mn^{2+} + O_2^{\bullet-} + 2H^+ \leftrightarrow Mn^{3+} + H_2O_2$	k_4 (s^{-1})	600	8×10^4
	k_{-4} ($M^{-1}s^{-1}$)	1×10^3	3×10^2

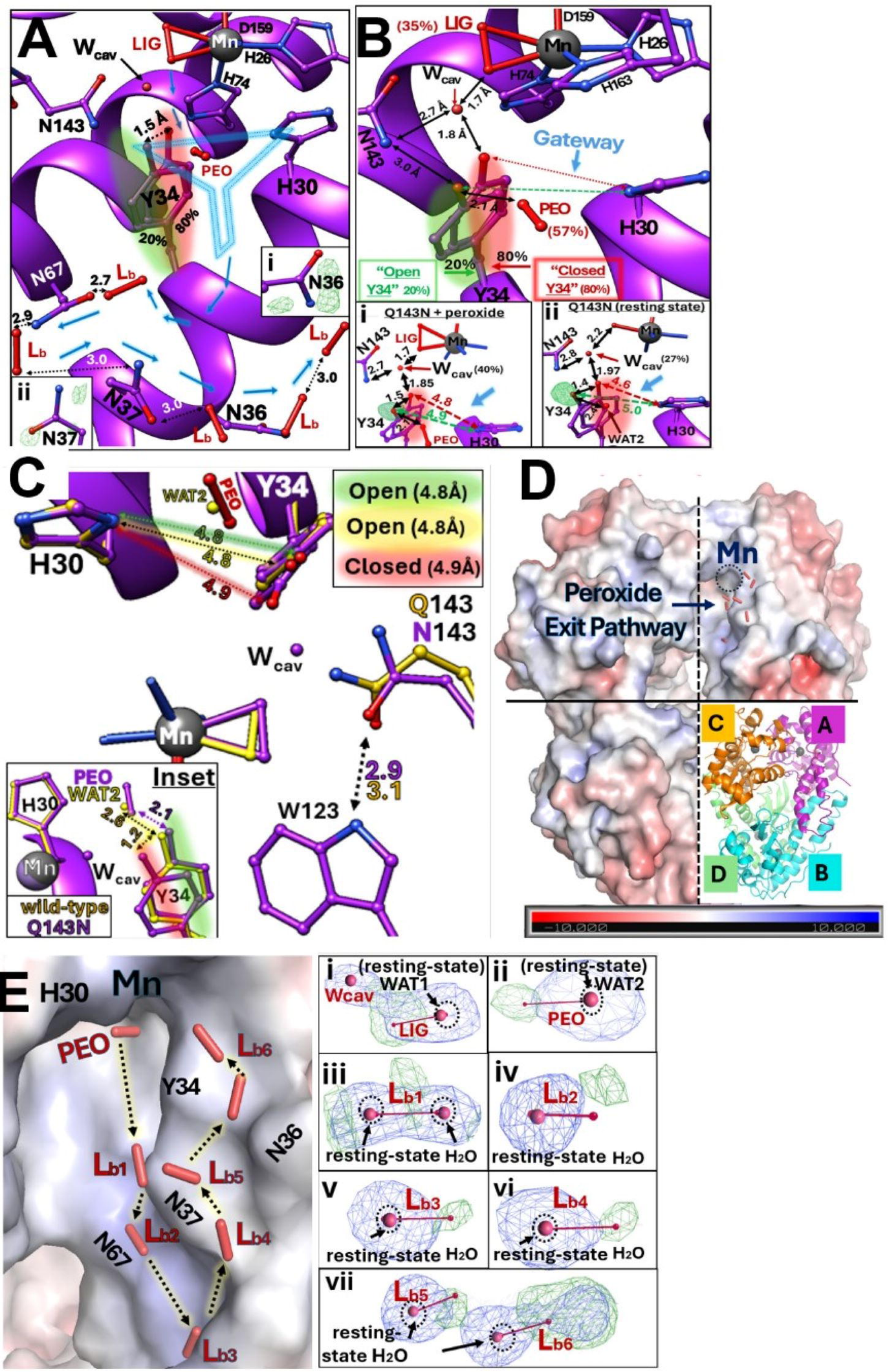
A
Wcav
LIG
Mn
D159
H26
H74
N143
1.5 Å
PEO
Y34
H30
80%
20%
N67
2.7
Lb
2.9
3.0
N37
N36
i
ii
B
(35%) LIG
D159
Mn
H26
H74
H163
Wcav
2.7 Å
1.7 Å
1.8 Å
Gateway
N143
3.0 Å
2.1 Å
PEO
(57%)
H30
20%
80%
"Open Y34" 20%)
"Closed Y34" (80%)
Y34
i Q143N + peroxide
N143
LIG
Mn
1.7
2.7
Wcav (40%)
1.85
1.5
4.8
4.9
Y34
PEO
H30
ii Q143N (resting state)
N143
2.2
Mn
2.8
Wcav (27%)
1.97
1.4
4.6
5.0
Y34
WAT2
H30
C
WAT2
PEO
Y34
H30
4.8
4.8
4.9
Open (4.8Å)
Open (4.8Å)
Closed (4.9Å)
Q143
N143
Wcav
Mn
2.9
3.1
W123
Inset
PEO
WAT2
H30
2.6
2.1
1.2
Mn
Wcav
Y34
wild-type
Q143N
D
Mn
Peroxide
Exit Pathway
C
A
D
B
-10,000
10,000
E
H30
Mn
PEO
Lb6
Y34
N36
Lb1
Lb5
N37
Lb2
Lb4
N67
Lb3
i (resting-state)
WAT1
Wcav
LIG
ii (resting-state)
WAT2
PEO
iii
Lb1
resting-state H2O
iv
Lb2
resting-state H2O
v
Lb3
resting-state H2O
vi
Lb4
resting-state H2O
vii
Lb5
resting-state H2O
Lb6

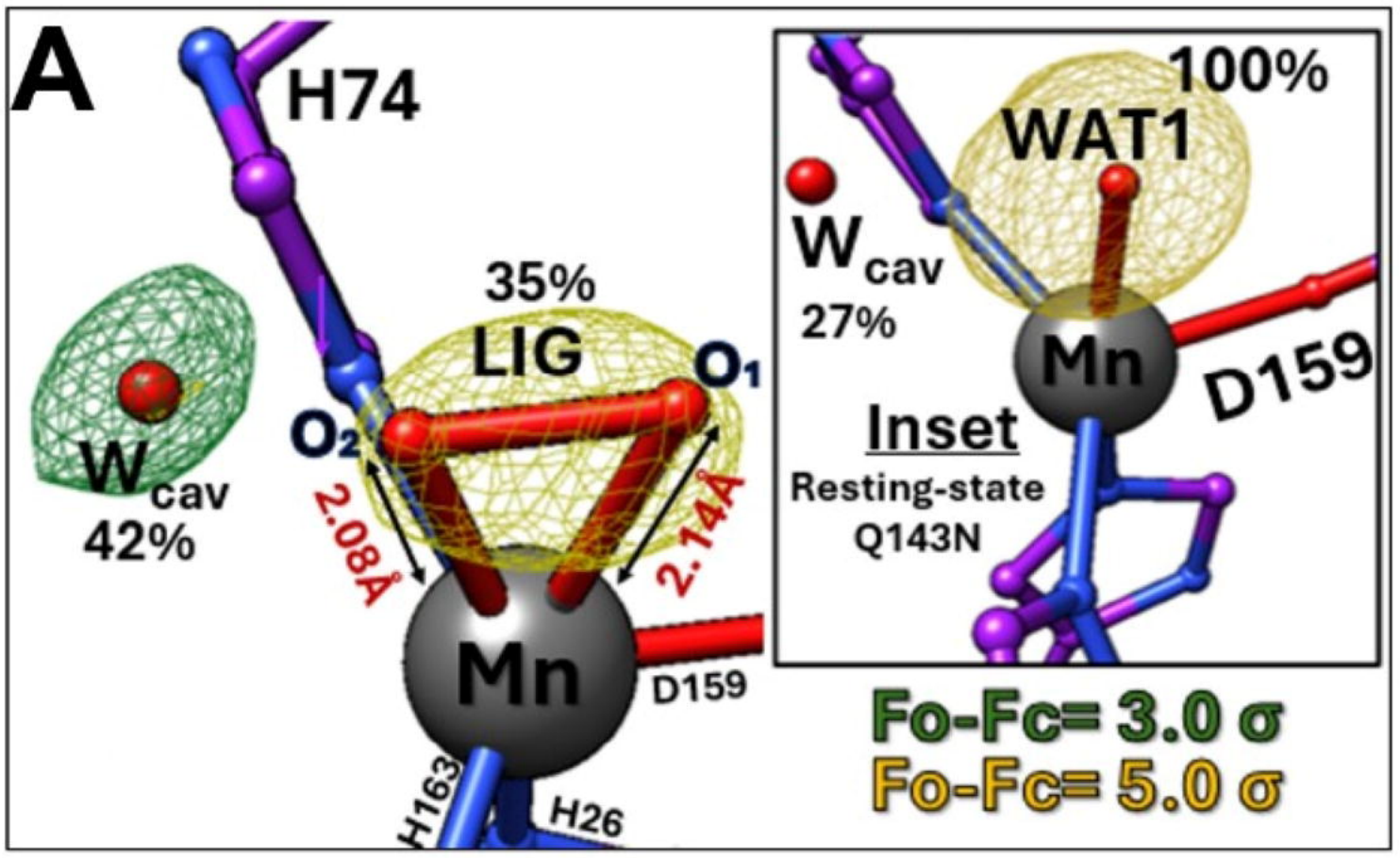

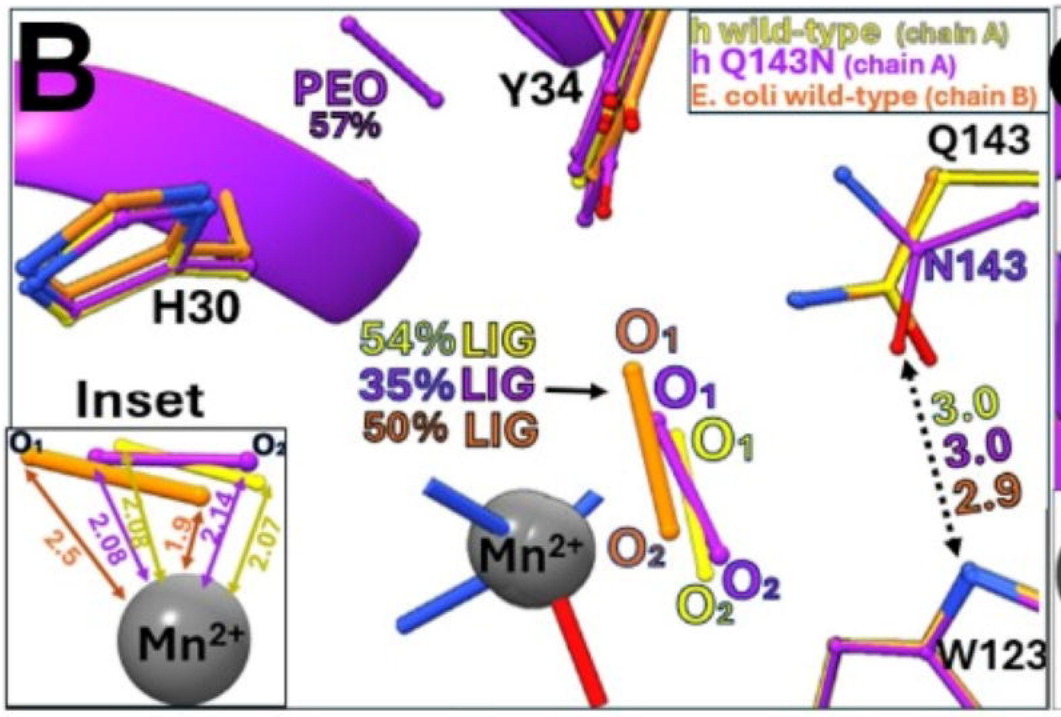

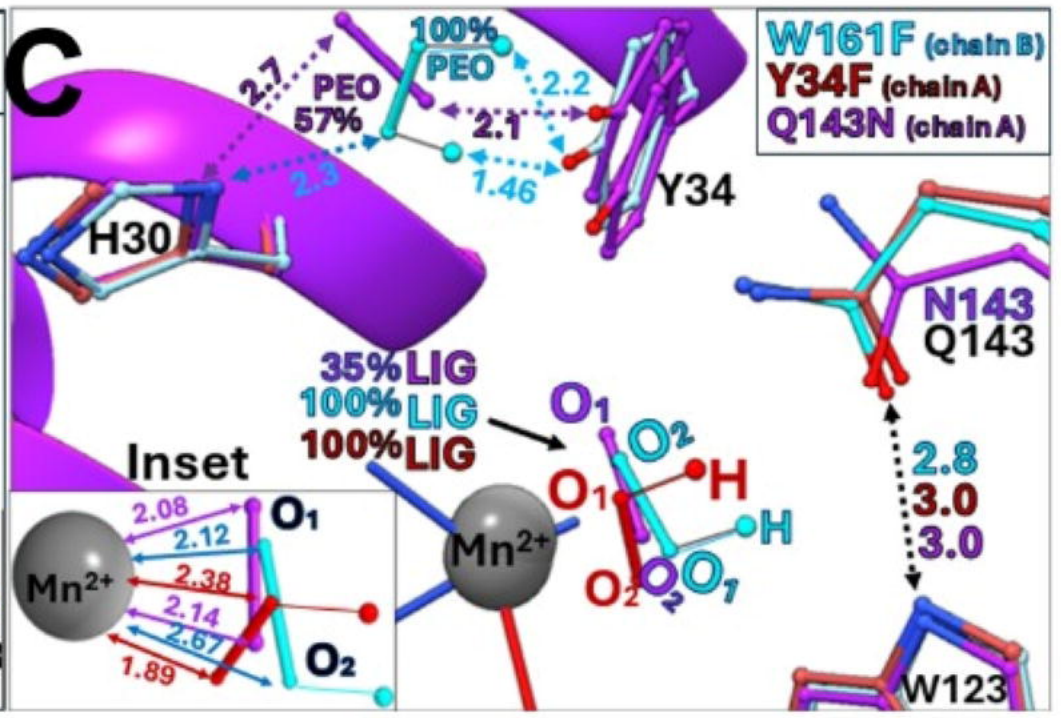

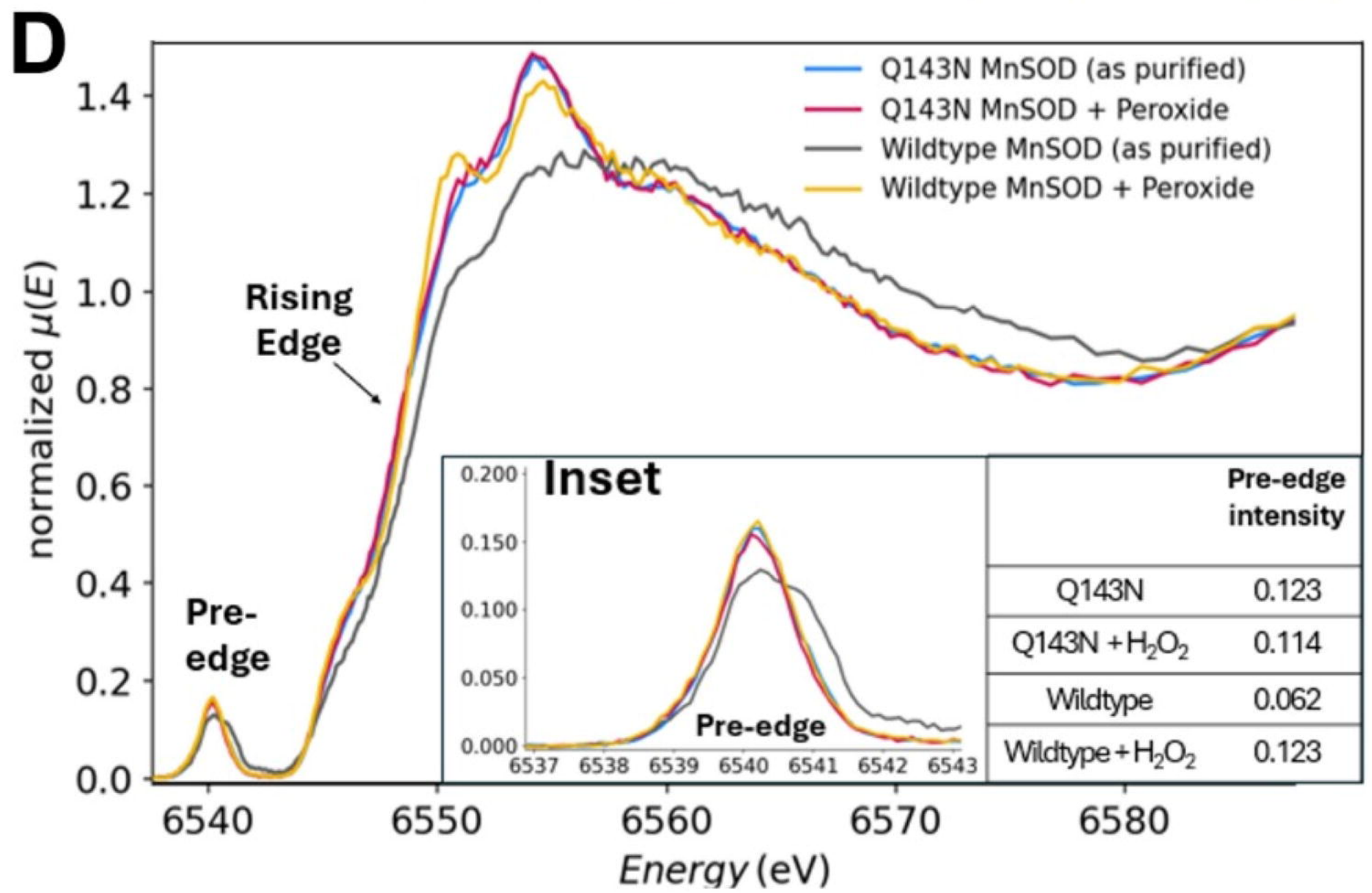

	Pre-edge intensity
Q143N	0.123
Q143N + H_2O_2	0.114
Wildtype	0.062
Wildtype + H_2O_2	0.123